ISSN 1063-7826, Semiconductors, 2018, Vol. 52, No. 1, pp. 44–52. © Pleiades Publishing, Ltd., 2018.
Original Russian Text © D.Yu. Protasov, A.K. Bakarov, A.I. Toropov, B.Ya. Ber, D.Yu. Kazantsev, K.S. Zhuravlev, 2018, published in Fizika i Tekhnika Poluprovodnikov, 2018, Vol. 52, No. 1, pp. 48–56.

SEMICONDUCTOR STRUCTURES, LOW-DIMENSIONAL SYSTEMS, AND QUANTUM PHENOMENA

Mobility of the Two-Dimensional Electron Gas in DA-*p*HEMT Heterostructures with Various δ–*n*-Layer Profile Widths

D. Yu. Protasov[a, b]*, A. K. Bakarov[a, c], A. I. Toropov[a, c], B. Ya. Ber[d], D. Yu. Kazantsev[d], and K. S. Zhuravlev[a, c]

[a] *Rzhanov Institute of Semiconductor Physics, Siberian Branch, Russian Academy of Sciences, Novosibirsk, 630090 Russia*
[b] *Novosibirsk State Technical University, Novosibirsk, 630073 Russia*
[c] *Novosibirsk State University, Novosibirsk, 630090 Russia*
[d] *Ioffe Institute, St. Petersburg, 194021 Russia*
** e-mail: protasov@isp.nsc.ru*

Submitted April 12, 2017; accepted for publication April 24, 2017

Abstract—The effect of the silicon-atom distribution profile in donor δ-layers of AlGaAs/InGaAs/AlGaAs heterostructures with donor–acceptor doping on the mobility of the two-dimensional electron gas is studied. The parameters of the δ-layer profiles are determined using the normal approximation of the spatial distributions of silicon atoms, measured by secondary-ion mass spectroscopy. It is shown that the standard deviation σ of the δ-layer profile can be reduced from 3.4 to 2.5 nm by the proper selection of growth conditions. Measurements of the magnetic-field dependences of the Hall effect and conductivity show that such a decrease in σ allowed an increase in the mobility of the two-dimensional electron gas in heterostructures by 4000 $cm^2/(V s)$ at 77 K and 600 $cm^2/(V s)$ at 300 K. The mobility calculation taking into account filling of the first two size-quantization subbands shows that an increase in the mobility is well explained by a reduction in the Coulomb scattering at ionized donors due to an increase in the effective thickness of the spacer layer with decreasing σ of the δ-layer profile.

DOI: 10.1134/S1063782618010189

1. INTRODUCTION

AlGaAs/InGaAs/AlGaAs pseudomorphic heterostructures are widely used to develop high-power high-frequency high electron mobility transistors (pseudomorphic high electron mobility transistors, *p*HEMTs). Since the first demonstration of *p*HEMT transistors [1], the *p*HEMT key parameters were significantly improved as a result of improvement in the design and growth technology of heterostructures. Double δ-doping made it possible to increase the two-dimensional electron gas (2DEG) density to 2×10^{12} cm^{-2} [2], to obtain sharp and smooth GaAs/InGaAs heterojunctions of a quantum well (QW), i.e., the transistor channel [3, 4], to determine the optimum distance between δ-layers and QWs [5, 6], to use composite spacer layers [7, 8], to use a wide-gap AlAs insert in QWs [9, 10], and to reliably attain an electron mobility above 7000 $cm^2/(V s)$ at room temperature. Despite all these significant efforts, the specific output power p_{out} of *p*HEMTs could not for a long time overcome the threshold of 1 W/mm in the frequency range of 10–30 GHz [11–13]. A radical increase in p_{out} occurred after the development of heterostructures with donor–acceptor doping (donor–acceptor doped *p*HEMT, DA-*p*HEMT) [14], which allowed an increase in p_{out} to 1.7 W/mm [15].

The additional doping of DA-*p*HEMT heterostructures results in a decrease in the electron mobility to 4500 $cm^2/(V s)$ at a density of 4×10^{12} cm^{-2} at 300 K [16]. The basic mechanism lowering the electron mobility is Coulomb scattering at ionized donors (silicon) [16] whose concentration is high, $(7–8) \times 10^{12}$ cm^{-2}, and which arrive at QWs due to δ-layer spreading during heterostructure growth due to diffusion and segregation processes [17, 18].

In this work, to optimize the DA-*p*HEMT heterostructure, the effect of the parameters of the spatial distribution of silicon atoms in δ layers on the electron mobility is calculated and experimentally studied.

2. SAMPLES AND EXPERIMENTAL

DA-*p*HEMT heterostructures were grown by molecular-beam epitaxy. A buffer layer consisting of a GaAs layer 0.4 μm thick and a GaAs/AlAs superlattice were grown on GaAs substrates; then, a heterostructure whose design is shown in Fig. 1a was grown. The growth rate and growth temperature for the $(Al_{0.25})GaAs$ and InGaAs layers were 0.28 nm s^{-1} and

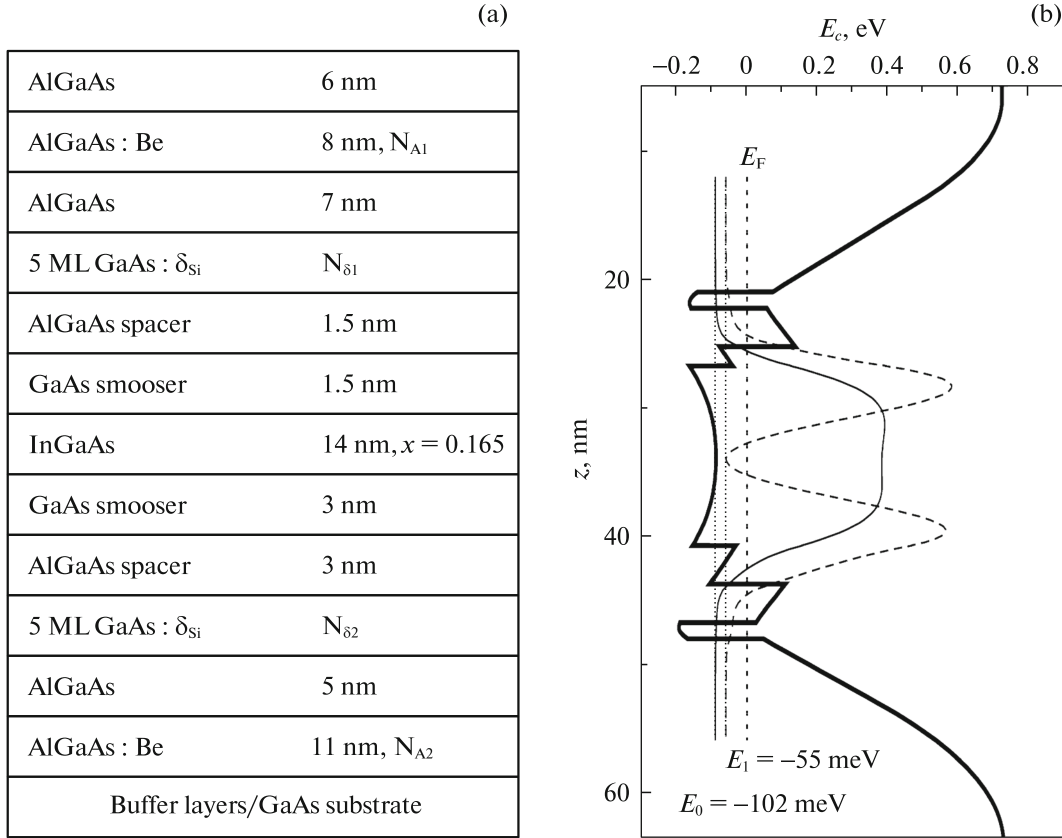

Fig. 1. DA-*p*HEMT heterostructure: (a) heterostructure design; (b) potential profile and the probability densities of finding electrons for two occupied size-quantization subbands for sample 1.

620°C, 0.24 nm s^{-1} and 500–520°C, respectively. δ layers were deposited at a temperature of 530°C. Two samples (1 and 2) differing in terms of the growth conditions of the spacer layers were studied.

The electron mobility and density were determined by measuring the magnetic-field dependences of the Hall effect and magnetoresistance using the van der Pauw method on samples 5 × 5 mm in size. The Hall effect and magnetoresistance were measured in the magnetic-field strength range of 0–2 T at temperatures of 300 and 77 K under direct current flowing through the sample. In this case, the maximum driving electric field did not exceed 0.5 V/cm. To determine the density and mobility of different types of electrons, the measured magnetic-field dependences of the Hall effect and magnetoresistance were analyzed using the mobility-spectrum method [19] in combination with multiband fitting [20].

In this method, the continuous distribution of the charge-carrier density on the charge-carrier mobility is described by a certain function $s(\mu)$ using which the conductivity tensor components $\sigma_{xx}(B)$ and $\sigma_{xy}(B)$ are determined in the form

$$\sigma_{xx}(B) = \int_{-\infty}^{\infty} \frac{s(\mu)d\mu}{1+\mu^2B^2}, \quad \sigma_{xy}(B) = \int_{-\infty}^{\infty} \frac{s(\mu)\mu B d\mu}{1+\mu^2B^2}. \quad (1)$$

This method allows determination of the function $s(\mu)$ as follows

$$s(\mu) = \sum_{i=1}^{n} \sigma_i \delta(\mu - \mu_i), \quad (2)$$

where σ_i is the conductivity of charge carriers with the mobility μ_i, $\delta(\mu - \mu_i)$ is the δ-function. The number of charge-carrier types is determined by the number of peaks in the mobility spectrum, and the charge-carrier density is determined by the peak area. The electron and hole mobilities are negative and positive, respectively. To improve the accuracy of determining the density and mobility of different charge-carrier types, the approximation of experimental values $\sigma_{xx}(B)$ and $\sigma_{xy}(B)$ by theoretical expressions for the conductivity tensor components is used. In the present study, such an approximation was performed by the least-squares method with minimization of the function Ψ by the Hooke–Jeeves method [21]. When processing the results of the Hall effect and magnetoresistance measurements for DA-*p*HEMT heterostructures, the minimized function Ψ in the general case depended on four variables: the density n_1 and mobility μ_{n1} of the 2DEG and the density n_2 and mobility μ_{n2} of electrons

in the layer parallel to the channel. In this case, the minimized function is written as

$$\Psi = \sum_i \left(\left(\frac{\sigma_{xx}^{\text{Exp}}(B_i) - \sigma_{xx}^{\text{Theo}}(B_i)}{\sigma_{xx}^{\text{Exp}}(B_i) + \sigma_{xx}^{\text{Theo}}(B_i)} \right)^2 + \left(\frac{\sigma_{xy}^{\text{Exp}}(B_i) - \sigma_{xy}^{\text{Theo}}(B_i)}{\sigma_{xy}^{\text{Exp}}(B_i) + \sigma_{xy}^{\text{Theo}}(B_i)} \right)^2 \right), \quad (3)$$

where the magnetic-field dependences of the conductivity tensor components are calculated by the formulas

$$\sigma_{xx}^{\text{Theo}}(B) = \sum_{i=1}^{2} \frac{qn_i\mu_i}{1 + \mu_i^2 B^2},$$
$$\sigma_{xy}^{\text{Theo}}(B) = \sum_{i=1}^{2} \frac{S_i qn_i\mu_i^2 B}{1 + \mu_i^2 B^2}, \quad (4)$$

where S_i is +1 (for holes) and −1 (for electrons). Similar equations are valid at the momentum relaxation time independent of the charge-carrier energy. In this case, the Hall factor is exactly unity.

The depth profiles of the basic (Al, Ga, In) and impurity (Be, Si) atoms were determined by dynamic SIMS using a CAMECA IMS-7f device. The Al, Ga, and In profiles were determined during sample bombardment with $^{133}Cs^+$ primary ions and measurements of secondary analytical diatomic ions such as $^{133}CsX^+$ (X = ^{27}Al, ^{69}Ga, ^{115}In). The Be depth profiles were determined during sample bombardment with $^{16}O_2^+$ primary ions and measurements of $^{9}Be^+$ secondary analytical ions. The Si depth profiles were determined during sample bombardment with $^{133}Cs^+$ primary ions and measurements of $^{28}Si^-$ secondary analytical ions; in this case, a high mass resolution $M/\Delta M \approx 4000$ was used to exclude mass interference of the analytical ion and $^{27}Al^1H^-$ secondary-ion signals. Quantitative analysis was performed using Si- and Be-doped GaAs samples.

3. THEORETICAL MODEL

In DA-*p*HEMT heterostructures, two size-quantization subbands (Fig. 1b) are occupied. Therefore, to calculate the 2DEG mobility in the samples under study, interband scattering was considered. In this case, the charge-carrier momentum relaxation time during elastic scattering in each size-quantization subband was expressed in terms of the scattering tensor components **K** and the subband energy-level positions E_i (i = 0.1) with respect to the Fermi level E_F. For the two occupied subbands, these expressions have the form [22]

$$\frac{1}{\tau_0} = \frac{K_{00}K_{11} - K_{01}K_{10}}{E_{F0}K_{11} - E_{F1}K_{01}}, \quad \frac{1}{\tau_1} = \frac{K_{00}K_{11} - K_{01}K_{10}}{E_{F1}K_{00} - E_{F0}K_{10}}, \quad (5)$$

where $E_{F_i} = E_F - E_i$, and the scattering tensor components are given by

$$K_{ij} = \delta_{ij}\sum_i K_{il}^{(1)} - K_{ij}^{(2)}, \quad (6)$$

$$K_{ij}^{(1)} = \frac{k_{Fi}^2}{2\pi\hbar}\int_0^\pi d\theta |V_{ij}(q_{ij})|^2, \quad (7)$$

$$K_{ij}^{(2)} = \frac{k_{Fi}k_{Fj}}{2\pi\hbar}\int_0^\pi d\theta \cos(\theta) |V_{ij}(q_{ij})|^2, \quad (8)$$

where the quasi-momentum change during scattering is $q_{ij} = (k_{Fi}^2 + k_{Fj}^2 - 2k_{Fi}k_{Fj}\cos(\theta))^{1/2}$ and $|V_{ij}(q)|^2$ is the squared matrix element of the corresponding scattering mechanism, expressions for which are given in [18]. Since expressions (5)–(8) are valid only for elastic-scattering mechanisms, the calculation was performed for a temperature of 77 K, when the effect of scattering on polar optical phonons can be neglected. Only scattering at charged donors, the deformation potential, and at alloy inhomogeneities was considered. Other scattering mechanisms (at charged acceptors, piezoelectric scattering, scattering at heterojunction roughnesses) are rather weak, their contribution to the resulting mobility is smaller than the ambiguity arising when choosing the parameters of stronger scattering mechanisms (deformation and alloy potentials) [18]. For all scattering mechanisms (long-range and short-range), screening was taken into account in the random phase approximation.

In calculating the mobility, first, according to Matthiessen's rule, the resulting mobility μ_i in the subbands was calculated and then the resulting mobility taking into account the subband occupations N_0 and N_1 were calculated,

$$\mu = \frac{N_0\mu_0 + N_1\mu_2}{N_0 + N_1}. \quad (9)$$

The potential diagrams and electron wave functions in the QWs were calculated by self-consistent solution of the Poisson and Schrödinger equations using the nextnano program [23]. The results of similar calculations for sample 1 at 77 K are shown in Fig. 1b.

4. RESULTS

4.1. Determination of the Dopant Depth Profile Parameters

Depth profiles of basic element atoms and dopant atoms for the heterostructure samples under study are shown in Figs. 2a and 2b. The QW position is identified by the distribution of indium atoms, GaAs and AlGaAs layers differ in terms of the Ga and Al atom concentration. The obtained distribution of basic ele-

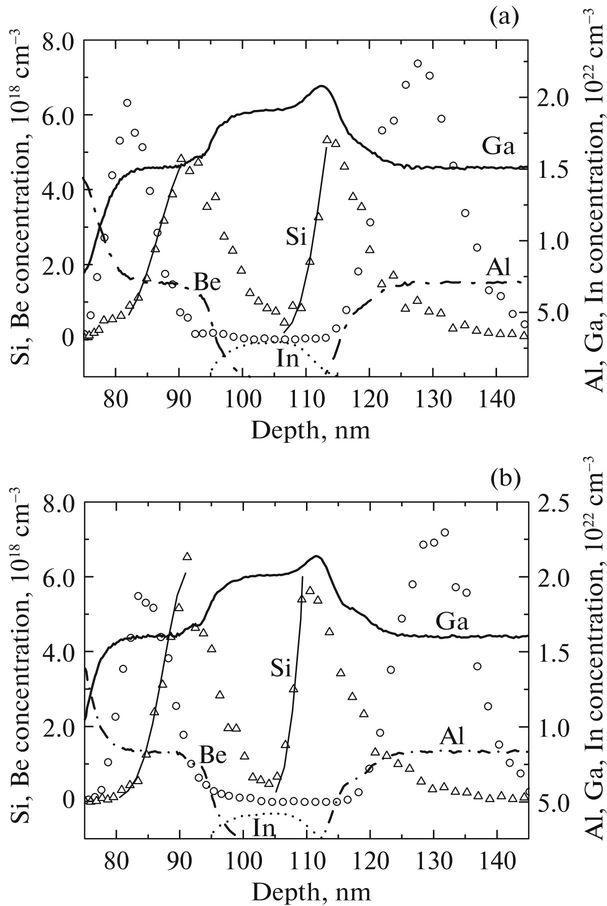

Fig. 2. Depth profiles of the atomic concentrations of the basic elements (Ga, Al, In are shown by solid, dash-dotted, and dashed curves, respectively) and dopant atoms (Be: circles, thin dashed curve, Si: triangles, thin solid curve). The Gaussian approximation for silicon is shown by a thin solid curve: (a) sample 1; (b) sample 2.

ments is consistent with the heterostructure design shown in Fig. 1. The beryllium-atom concentration in the QW region does not exceed 4×10^{16} cm^{-3}, which allows one to speak about the practically complete absence of this impurity in the DA-*p*HEMT heterostructure channel. The silicon depth profiles in the δ layers and beryllium in the AlGaAs layers are rather strongly broadened and asymmetric: the side closest to the surface is sharper than the side adjacent to the substrate.

Profile broadening is caused by impurity segregation and diffusion during heterostructure growth, and the extended profile is caused by impurity-atom displacement during material sputtering by primary ions, i.e., the so-called "knock-on" effect, and does not correspond to the actual impurity profile.

The obtained impurity-atom distributions were approximated by Gaussian curves

$$N_i(z) = N_i/\sqrt{2\pi\sigma^2}\exp(-(z - z_{ci})^2/(2\sigma_i^2)), \qquad (10)$$

where σ_i is the standard deviation and z_{ci} is the distribution maximum in the i-th doping layer; N_i is the total impurity concentration. To eliminate the "knock-on" effect, only the leading edges of the distributions were analyzed. Expression (10) contains three fitting parameters. To reduce the number of simultaneously determined variables and to improve the approximation accuracy, the concentration N_i was determined independently by numerical integration of the dependences shown in Fig. 2. Furthermore, integration made it possible to eliminate both the "knock-on" effect on N_i and sample etching nonuniformities. Then, using expressions (10), an objective function similar to expression (3), which was minimized by the least-squares method according to the Hooke–Jeeves algorithm [21] using σ_i and z_{ci} as varied parameters, was constructed. The parameters of the donor distribution profile in σ layers, obtained in such a way, are shown in Table 1.

To estimate the reliability of the obtained parameters, the set and measured distances between the doped layers were compared. According to Fig. 1a, the distance between the δ layers in the heterostructures should be 25.8 nm (at a GaAs single-layer thickness of 0.28 nm); the distance between the acceptor-layer centers should be 49.2 nm. For the samples under study, the distance between the δ layers was calculated using the impurity distribution parameters given in Table 1. For samples 1 and 2, the distances obtained are 24 and 21 nm. The distances between the acceptor-layer centers, determined by Fig. 2a and 2b, are 46 nm for both samples. These values are in rather good agreement with the set values. The results of the study of a sample by high-resolution transmission microscopy, given in [16], yield a distance between δ layers of 26.8 nm which is close to the above values. The silicon concentration in the δ layers for both samples is also in good agreement with the set value of (6–7) × 10^{12} cm^{-2}.

Table 1. Parameters of the donor distribution profile

Parameter	Sample 1		Sample 2	
	upper δ layer	lower δ layer	upper δ layer	lower δ layer
Total concentration N_i, 10^{12} cm^{-2}	6.3	6.1	5.8	5.9
Standard deviation σ_i, nm	5.0	3.4	3.9	2.5
Profile peak position z_{ci}, nm	92	116	91	112

Hence, the electrical activation coefficient of silicon is almost 100% which is consistent with the results of [24] in which complete silicon activation was observed up to an atomic concentration of 10^{13} cm^{-2}.

It is rather difficult to estimate the reliability of determination of the standard deviation. Simple estimation by the profile half-width at half maximum (PHWHM) yields 3.7 nm/5.9 nm and 3.4 nm/5.9 nm for the upper and lower acceptor layers for samples 1 and 2, respectively. When using the normal distribution to approximate the acceptor profiles, we obtain standard deviations of 3.1 nm/5.4 nm and 3.7 nm/5.6 nm for the upper and lower layers of samples 1 and 2, respectively. The PHWHM is related to the standard deviation by the simple relation $h = \sqrt{2\ln 2}\sigma \approx 1.177\sigma$. Hence, these estimates of σ by the PHWHM and the fitting data for the acceptor layers are in good agreement with each other. For δ-*n* layers, such simple estimation yields significantly different results, 4.3 nm/2.5 nm and 3.4 nm/2.3 nm for the upper and lower δ layers of sample 1 and 2, respectively. Such a difference from the values given in Table 1 can be explained by the fact that it is rather difficult to determine the peak position of the impurity distribution in a very thin layer, since it is strongly distorted during measurements due to the "knock-out" effect. The maximum difference between the results of simple estimation and fitting allows estimation of the range of possible values of the standard deviation of the δ-layer profile as ±0.4 nm from the values given in Table 1.

As is known, ionized atoms arranged closer to QWs have a significant effect on the 2DEG mobility. Such atoms are on the right slope of the upper profile and on the left slope of the lower profile of the silicon-atom distribution in the δ layers. However, the standard deviation σ_i was determined only for the left slopes of the lower δ layers. It follows from Figs. 2a and 2b and Table 1 that σ_i for the left slope of the δ layer for both samples is larger than that of the corresponding slope of the lower δ layer. Since these layers were grown at the same temperature, the cause of such a phenomenon is unclear. Meanwhile, the distribution of impurity atoms in the δ layer should be asymmetric, since impurity atoms propagate against the growth direction (right slopes) only due to diffusion; propagation in the growth direction (left slopes) occurs due to both impurity diffusion and segregation.

Hence, it can be assumed that the standard deviation for the right slope of the upper δ layer does not exceed the value obtained for the left slope of the lower δ layer. Therefore, in what follows, the 2DEG mobility was calculated using identical standard deviations for both δ layers, equal to σ_i for the left slope of the lower δ layer.

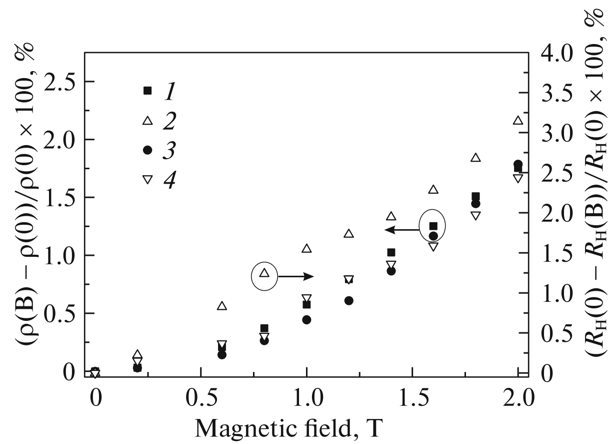

Fig. 3. Relative changes in the Hall effect and resistivity in a magnetic field for sample 2. Numerals indicate (*1*) Δρ, (*2*) ΔR_H, (*3*) Δρ, (*4*) ΔR_H for 77 and 300 K, respectively.

4.2. Electron Density and Mobility Determination

To determine the experimental values of the 2DEG mobility in the samples under study, the contribution of the parallel conducting channel to the conductivity should be separated. This will make it possible to correctly compare the experimental and calculated 2DEG mobilities. To this end, the magnetic-field dependences of the Hall effect and resistivity were measured. In the studied DA-*p*HEMT heterostructures, both the Hall effect and resistivity vary insignificantly with increasing magnetic-field strengths from 0 to 2 T. Figure 3 shows the relative changes in the Hall coefficient R_H and resistivity ρ in sample 2 at 77 and 300 K. We can see in this figure that the change in these values does not exceed 3.5%. In conventional *p*HEMT heterostructures, the magnetoresistance is larger by an order of magnitude [16].

The positive magnetoresistance and Hall coefficient nonlinearity in a magnetic field can result from the following: (i) the energy dependence of the relaxation time, (ii) the existence of several charge-carrier groups, (iii) constant energy surface asphericity, (iv) the presence of several equivalent energy minima, (v) the presence of foreign inclusions (including magnetic ones), (vi) the effect of the sample geometry [25, 26]. Since GaAs is a direct-gap single-valley semiconductor with a spherical Fermi surface, whose growth technology is well developed, only the first two factors are significant. The first factor plays a role in nondegenerate semiconductors where charge carriers obey Boltzmann statistics, and their energies are in a relatively wide range of values. Due to the energy dependence of the momentum-relaxation time, charge carriers have different mobilities (or drift velocities); therefore, the Hall electric field cannot compensate for the Lorentz force. In degenerate semiconductors which obey Fermi–Dirac statistics, charge carriers with energies lying in a rather narrow gap $\pm k_B T$ near

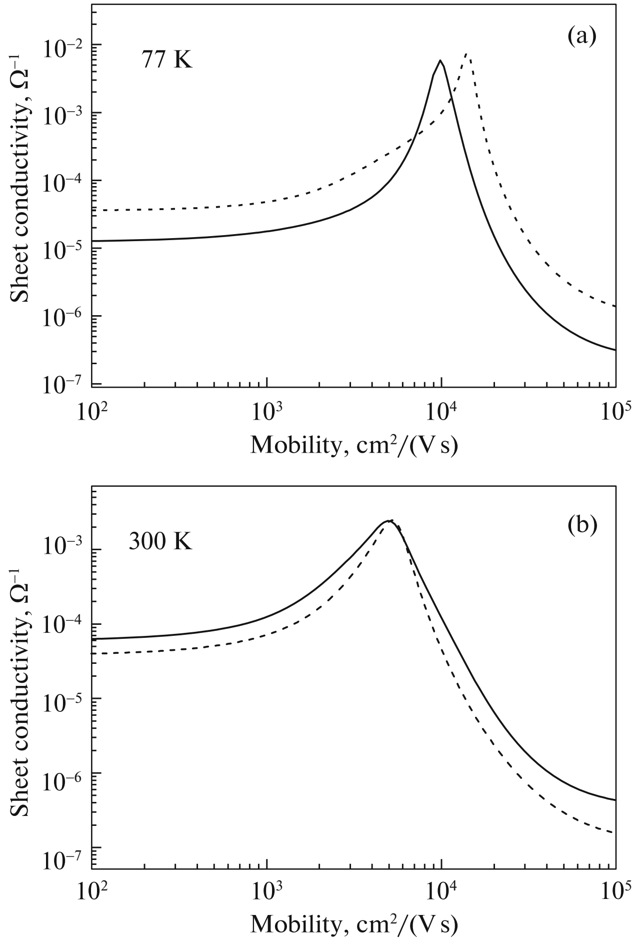

Fig. 4. Mobility spectra for electrons in samples 1 (solid curves) and 2 (dashed curves) at temperatures of (a) 77 and (b) 300 K.

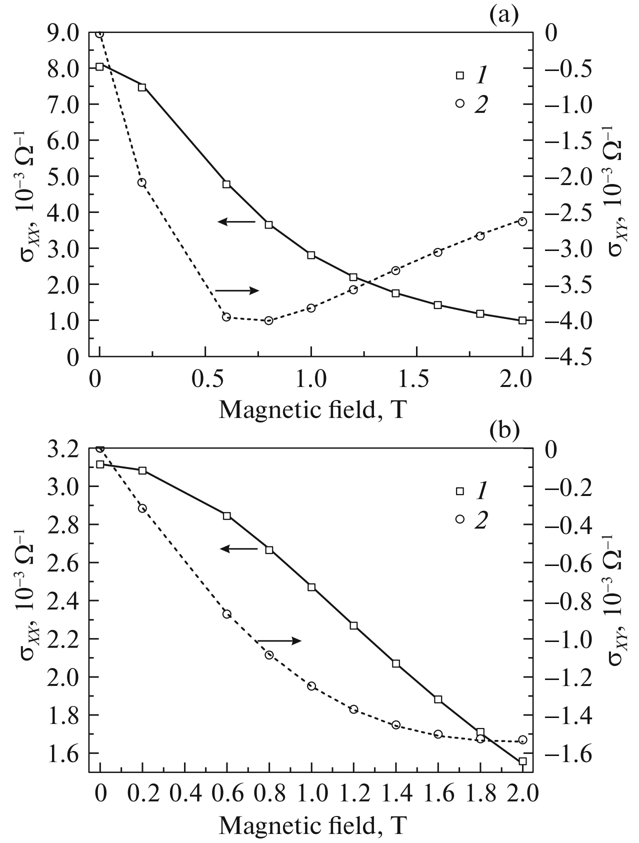

Fig. 5. Dependence of the conductivity tensor components on the magnetic field for sample 2 at temperatures of (a) 77 and (b) 300 K. Numerals indicate the experimental values: (*1*) σ_{xx}, (*2*) σ_{xy}. Curves are the results of two-band fitting for σ_{xx} (solid curve) and σ_{xy} (dashed curve).

the Fermi level are involved in conductivity. Therefore, the difference between the mobilities of such carriers is small and the positive magnetoresistance is also small. Its value can be estimated using the expression [27]

$$\frac{\Delta\rho}{\rho_0} = \frac{\pi^2}{12}\,\frac{(\mu B)^2}{1+(\mu B)^2}\left(\frac{k_B T}{E_F}\right)^2, \qquad (11)$$

where ρ_0 is the resistivity in the absence of magnetic field. In the samples under study, 2DEG is degenerate even at room temperature, since its concentration is on the order of 4×10^{12} cm^{-2}, which significantly exceeds the degeneracy condition $m^*kT/\pi\hbar^2 \approx 7 \times 10^{11}$ cm^{-2}. The calculation by expression (11) for the mobility μ = 15 000 cm^2/(V s), the magnetic-field strength B = 2 T, a temperature of 77 K, and the Fermi-level position E_F = 100 meV, yields a relative magnetoresistance of 0.3%. The magnetoresistance of the samples studied is significantly higher, 1.5–2.0% (see Fig. 3); therefore, we relate these changes in the resistivity and Hall coefficient to weak parallel conductance which is conventionally related to the conductance over the region of δ layers [28].

To estimate the parallel conductance, the magnetic-field dependences of the Hall effect and resistivity (or conductance) were processed by the mobility spectrum method. Figures 4a and 4b show the calculated spectra of the electron mobility at 77 and 300 K, respectively.

One peak is clearly seen in all spectra, which is located in the region of mobilities characteristic of 2DEG mobility. There are no additional peaks reflecting the effect of parallel conductance in the mobility spectra. We note that parallel conductance peaks in ordinary *p*HEMT heterostructures in the mobility spectra are pronounced [16]. As seen in the figures, the 2DEG mobility at 77 K in the sample 1 μ_1 = 10 000 cm^2/(V s) is appreciably lower than the mobility in sample 2, μ_2 = 14 000 cm^2/(V s). As the temperature increases to 300 K, the difference between the mobilities of the samples under study becomes appreciably lower, μ_1 = 4900 cm^2/(V s) for sample 1 and μ_2 =

Table 2. Electron density and mobility in DA-pHEMT layers of heterostructures

Sample no.	Temperature, K	2DEG		Parallel conducting layer	
		μ, $cm^2/(V s)$	$10^{12}n$, cm^{-2}	μ, $cm^2/(V s)$	$10^{12}n$, cm^{-2}
1	77	10070 ± 50	3.87 ± 0.02	2800 ± 200	0.33 ± 0.03
	300	4600 ± 50	4.01 ± 0.06	1700 ± 420	0.39 ± 0.05
2	77	14030 ± 65	3.52 ± 0.03	5600 ± 810	0.34 ± 0.03
	300	5200 ± 40	3.59 ± 0.04	1900 ± 350	0.42 ± 0.02

Table 3. Calculated 2DEG mobilities in DA-pHEMT heterostructures at 77 K

Sample no.	Subband	Scattering mechanisms limiting the mobility			Resulting sample mobility, $cm^2/(V s)$
		charged donors, $cm^2/(V s)$	deformation potential, $cm^2/(V s)$	alloy inhomogeneity, $cm^2/(V s)$	
1	1 subband	11334	82267	84883	8825
	2 subband	12044	78584	106930	9420
					9070
2	1 subband	17375	80385	82773	12184
	2 subband	18828	75402	103836	13356
					12648

5300 $cm^2/(V s)$ for sample 2. The conductivity in the mobility spectral region corresponding to holes is less than 10^{-5} Ω^{-1}, which indicates the absence of conductivity over p^+ layers.

To determine more accurate densities and mobilities of 2DEG and electrons in the parallel conducting layer, the objective function (3) was minimized. The experimental magnetic-field dependences of the conductivity tensor and those calculated using such an analysis $\sigma_{xx}(B)$ and $\sigma_{xy}(B)$ for sample 2 are shown in Figs. 5a and 5b for temperatures of 77 and 300 K, respectively. Similar results were obtained for sample 1.

We can see that the use of two types of electrons allows adequate description of the magnetic-field dependences of the conductivity-tensor components. The obtained electron densities and mobilities are given in Table 2. The errors of the obtained parameters were determined statistically by results of no less than 300 minimizations; therefore, they reflect only the objective-function-minimization error (3).

4.3. 2DEG Mobility Calculation

To calculate the 2DEG mobility, the following values of the root-mean-square deviation of the silicon distribution profile in δ layers were used: 3.4 nm for sample 1 and 2.5 nm for sample 2. The mobility calculation results at a temperature of 77 K are listed in Table 3.

The calculated results show that the 2DEG mobility in DA-pHEMT heterostructures at low temperatures is limited by scattering at charged donors. The mobility of electrons in two occupied subbands differs weakly. Therefore, in the analysis of the magnetic-field dependences of the Hall effect and magnetoresistance, these electrons do not appear as separate peaks in the mobility spectrum.

5. DISCUSSION

The 2DEG mobility in sample 2 upon a decrease in temperature from 300 to 77 K increased to a greater degree than in sample 1. Therefore, it could be argued that the effect of scattering at charged donors, which dominates at low temperatures, decreased in sample 2. This is due to an increase in the effective spacer-layer width, since the standard deviation of the δ-layer profile is 2.5 nm in sample 2 and 3.4 nm in sample 1. Then, at the same spacer-layer thickness, the distance from the δ layers to the 2DEG in sample 2 will be larger than in sample 1. At room temperature, scattering at ionized donors is the second largest after scattering at polar optical phonons [18]; therefore, its effect is weaker. and the difference between the 2DEG mobilities in samples 2 and 1 is smaller.

The calculated total DEG mobilities (see Table 3) obtained using the δ-layer parameters are in good agreement with the experimental 2DEG mobilities from Table 2 for $T = 77$ K. Thus, it was experimentally and theoretically shown that a decrease in the DA-pHEMT δ-layer spreading leads to an increase in the 2DEG mobility. Certainly, achieving complete

agreement between the theoretical and experimental 2DEG mobilities could be attempted by varying the standard deviation of the δ layers within the range of ±0.4 nm estimated above. The dependence of the 2DEG mobility on the standard deviation, given in [18], shows that the mobility can be increased by 1000 $cm^2/(V s)$ for sample 1 and by 2000 $cm^2/(V s)$ for sample 2 by such σ variation. At the same time, the calculated mobilities can also be matched with experimental choice of the deformation potential D and the alloy potential E_D defining the scattering intensity on the deformation potential and the alloy potential, respectively. For example, when varying the alloy potential in the range of 0.51–1.15 eV, which is given for InGaAs in [29], the mobility limited by scattering at alloy inhomogeneities will vary from 23000 to 45000 $cm^2/(V s)$. Similarly, a large spread is inherent for the deformation potential: from −6.3 to −18.3 eV for GaAs and from −5.1 to −11.7 eV for InAs [30]. Therefore, such matching of the mobilities is beyond the scope of this paper.

6. CONCLUSIONS

The effect of the spatial distribution of dopant atoms in (δ-layers of DA-*p*HEMT heterostructures on the 2DEG mobility was studied to optimize these heterostructures. The spatial distribution of dopants (silicon and beryllium) in DA-*p*HEMT heterostructures was determined by the SIMS method. The total silicon concentration in the δ layers and their arrangement are in quite good agreement with those specified during growth. To determine the δ-layer profile width, the silicon-atom distributions were approximated by a normal distribution; as a result the standard deviations σ were determined. It was shown that σ was decreased from 3.4 to 2.5 nm by choosing the growth conditions. The beryllium-atom concentration in the QW region does not exceed 4×10^{16} cm^{-3} which is at the SIMS limit of detection; therefore, Be atoms barely penetrate the channel of DA-*p*HEMT heterostructures.

The 2DEG mobility in DA-*p*HEMT heterostructures was determined by analyzing the magnetic-field dependences of the Hall effect and conductivity by the mobility spectrum method, and was refined using the two-band mixed conductivity model. It should be noted that, despite the high 2DEG density (~4×10^{12} cm^{-2}), parallel conductance is almost lacking in DA-*p*HEMT heterostructures: the electron density in the parallel conducting layer does not exceed 11% of the 2DEG density, and the electron mobility is lower than the 2DEG mobility by a factor of more than 2.5.

It was found that as the δ-layer width decreases, the 2DEG mobility increases by 4000 $cm^2/(V s)$ at 77 K and by 600 $cm^2/(V s)$ at 300 K. The 2DEG mobility calculation performed taking into account the filling of two size-quantization bands in DA-*p*HEMT heterostructures, allows the conclusion that this difference is associated with a reduction in scattering at charged donors due to a decrease in the standard deviation of the δ-layer profile from 3.4 to 2.5 nm.

ACKNOWLEDGMENTS

SIMS measurements were performed at the Shared service center "Materials Science and Diagnostics in High Technologies" (Ioffe Physical–Technical Institute), supported by the Ministry of Education and Science of Russia.

REFERENCES

1. A. Ketterson, M. Moloney, W. T. Masselink, C. K. Peng, J. Klem, R. Fischer, W. Kopp, and H. Morkoc, IEEE Electron Dev. Lett. **6**, 628 (1985).
2. M. Kudo, T. Mishima, T. Tanimoto, and M. Washima, Jpn. J. Appl. Phys. **33**, 971 (1994).
3. K.-J. Chao, N. Liu, C.-K. Shih, D. W. Gotthold, and B. G. Streetman, Appl. Phys. Lett. **75**, 1703 (1999).
4. H. Toyoshima, T. Niwa, J. Yamazaki, and A. Okamoto, J. Appl. Phys. **75**, 3908 (1994).
5. Y. C. Chen and P. K. Bhattacharya, J. Appt. Phys. **73**, 7389 (1993).
6. B. Jogai, Appl. Phys. Lett. **66**, 436 (1995).
7. K. Inoue, H. Sakaki, J. Yoshino, and Y. Yoshioka, Appl. Phys. Lett. **46**, 973 (1985).
8. A. N. Vinichenko, V. P. Gladkov, N. I. Kargin, M. N. Strikhanov, and I. S. Vasil'evskii, Semiconductors **48**, 1619 (2014).
9. J. Požela, V. Juciene, and K. J. Požela, Semicond. Sci. Technol. **10**, 1076 (1995).
10. V. G. Mokerov, G. B. Galiev, J. Požela, K. Požela, and V. Juciene, Semiconductors **36**, 674 (2002).
11. C. H. Lin, H. Z. Liu, C. K. Chu, H. K. Huang, Y. H. Wang, C. C. Liu, C. H. Chang, C. L. Wu, and C. S. Chang, in *Proceedings of the Compound Semiconductor Integrated Circuit Symposium, San-Antonio, TX, Nov. 12–15, 2006*, p. 165.
12. H. Amasuga, Seiki Goto, T. Shiga, and M. Totsuka, in *Proceedings of the IEEE MTT-S International Microwave Symposium, Long Beach, CA, June 11–17, 2005*, p. 831.
13. D. C. Dumka, Ming-Yih Kao, Edward Beam, Tso-Min Chou, Hua-Quen Tserng, and D. M. Fanning, in *Proceedings of the Compound Semiconductor Integrated Circuit Symposium, Monterey, CA, Oct. 3–6, 2010*, p. 188.
14. V. M. Lukashin, A. B. Pashkovskii, K. S. Zhuravlev, A. I. Toropov, V. G. Lapin, and A. B. Sokolov, Tech. Phys. Lett. **38**, 819 (2012).
15. V. M. Lukashin, A. B. Pashkovskii, K. S. Zhuravlev, A. I. Toropov, V. G. Lapin, E. I. Golant, and A. A. Kapralova, Semiconductors **48**, 666 (2014).

16. D. V. Gulyaev, K. S. Zhuravlev, A. K. Bakarov, A. I. Toropov, D. Yu. Protasov, A. K. Gutakovskii, B. Ya. Ber, and D. Yu. Kazantsev, J. Phys. D: Appl. Phys. **49**, 095108 (2016).
17. E. H. Hwang and S. Das Sarma, Phys. Rev. B **77**, 235437 (2008).
18. D. Yu. Protasov and K. S. Zhuravlev, Solid State Electron. **129**, 66 (2017).
19. W. A. Beck and J. R. Anderson, J. Appl. Phys. **62**, 541 (1987).
20. D. Yu. Protasov, A. V. Trifanov, and V. Ya. Kostyuchenko, Eur. Phys. J. Appl. Phys. **62**, 30104 (2013).
21. T. E. Shoup, *A Practical Guide to Computer Methods for Engineers* (Prentice-Hall, Upper Saddle River, NJ, 1979; Mir, Moscow, 1982).
22. R. Fletcher, E. Zaremba, M. D'Iorio, C. T. Foxon, and J. J. Harris, Phys. Rev. B **41**, 10649 (1990).
23. Software for Semiconductor Nanodevices, www.nextnano.de. Accessed April 25, 2017.
24. E. F. Schubert, L. Pfeiffer, K. W. West, H. S. Luftman, and G. J. Zydzik, Appl. Phys. Lett. **64**, 2238 (1994).
25. E. V. Kuchis, *Galvanomagnetic Effects and Methods of their Study* (Radio Svyaz', Moscow, 1990) [in Russian].
26. A. C. Beer, *Galvanomagnetic Effects in Semiconductors* (Academic, New York, London, 1963).
27. P. S. Kireev, *Semiconductor Physics* (Vyssh. Shkola, Moscow, 1975) [in Russian].
28. G. B. Galiev, I. S. Vasil'evskii, E. A. Klimov, V. G. Mokerov, and A. A. Cherechukin, Semiconductors **40**, 1445 (2006).
29. D. Chattopadhyay, S. K. Sutradhar, and B. R. Nag, J. Phys. C **14**, 891 (1981).
30. I. Vurgaftman, J. R. Meyer, and L. R. Ram-Mohan, J. Appl. Phys. **89**, 5815 (2001).

Translated by A. Kazantsev